

Article

Investigation on the Confined Breakage Characteristics of Calcareous Sand in the South China Sea Integrated Using Relative Breakage Ratio and Fractal Dimension

Jianfeng Zhu ¹ , Qiqi Zheng ¹ and Hao Yang ^{1,2,*}

¹ School of Civil Engineering and Architecture, Zhejiang University of Science and Technology, Hangzhou 310023, China; zhujianfeng@zust.edu.cn (J.Z.); 212102814013@zust.edu.cn (Q.Z.)

² Institute of Geotechnical Engineering (IGT), University of Natural Resources and Life Sciences, Feistmantelstrasse 4, 1180 Vienna, Austria

* Correspondence: 212002814020@zust.edu.cn; Tel.: +86-15705820186

Abstract: Calcareous sand, ubiquitous in the geotechnical makeup of the South China Sea, exhibits both compressibility and vulnerability to fragmentation when subjected to external loading, spanning a spectrum from typical to extreme conditions. This investigation aims to quantitatively assess the compression and particle breakage characteristics of calcareous sand under varied parameters, including relative density, saturation, applied loads, and loading paths, specifically focusing on sustainable geotechnical methodologies. Through a series of confined compression tests, this evaluation employed the relative breakage ratio and fractal dimension as key evaluative metrics. The results indicated that employing this integrated approach offered a more comprehensive understanding of calcareous sand breakdown mechanisms than relying on a singular particle breakage index. Furthermore, an increase in relative density can induce a transition in particle contact behavior, shifting from point-to-point interactions to face-to-face contact, thereby reducing inter-particle stress and minimizing grain breakage, particularly under loads below 200 kPa. Increasing loads exacerbated particle breakage, with finer particles predominantly initiating this process. During reloading, pore ratios across various load levels surpass those observed during initial loading, except at 1600 kPa, where a decline in pore ratio was noted, coinciding with pore water extrusion and the onset of new particle fracturing. The lubricating effect of water reduces inter-particle friction, enhancing stress concentration at particle edges and localized particle breakage, thereby increasing the presence of finer particles without significantly altering the overall structure. Notably, the influence of pore water pressure is evident during the reloading phase. These findings contribute to a refined theoretical framework for predicting coastal erosion risks and devising effective environmental protection strategies for sustainable coastal engineering practices.



Citation: Zhu, J.; Zheng, Q.; Yang, H. Investigation on the Confined Breakage Characteristics of Calcareous Sand in the South China Sea Integrated Using Relative Breakage Ratio and Fractal Dimension. *Sustainability* **2024**, *16*, 2190. <https://doi.org/10.3390/su16052190>

Academic Editor: Md. Mizanur Rahman

Received: 1 February 2024

Revised: 27 February 2024

Accepted: 4 March 2024

Published: 6 March 2024

Keywords: calcareous sand; particle breakage; relative breakage ratio; fractal dimension; compression behavior

1. Introduction

Calcareous sand, abundant in the South China Sea and originating from marine organisms like corals and shells, mainly consists of insoluble carbonates, particularly calcium carbonate [1–3]. Its extensive utilization as a construction filler in island development encompasses a variety of applications, including foundations [4], roadbeds [5], and airport runways [6]. The irregular shapes, dense pore structure, inadequate gradation, and low particle strength collectively contribute to the distinct compression and crushing properties of this material [7–14].

The distinctive nature of calcareous sand plays a pivotal role in coastal environments. The fragmentation of these sand particles has a profound impact on coastal erosion and



Copyright: © 2024 by the authors. Licensee MDPI, Basel, Switzerland. This article is an open access article distributed under the terms and conditions of the Creative Commons Attribution (CC BY) license (<https://creativecommons.org/licenses/by/4.0/>).

overall coastal stability [15,16]. Fragmentation leads to a reduction in grain size, a notable increase in sediment mobility, and an exacerbation of vulnerability to erosion. These consequences pose significant challenges to both shoreline integrity and ecological equilibrium [17]. Moreover, it amplifies the risk of sediment displacement and coastal erosion, potentially resulting in adverse outcomes such as shoreline retreat as well as geological hazards like landslides or collapses [18]. Furthermore, this disruption induces alterations in sediment dynamics within nearshore areas, with the potential to reshape seabed structures and geomorphological features [19]. Therefore, understanding the implications of calcareous sand particle fragmentation is crucial for effective coastal management, planning, and sustainable development. A comprehensive understanding of these mechanisms is essential for devising robust strategies in coastal engineering, environmental preservation, and disaster mitigation. Precise insights into sand particle fragmentation significantly contribute to accurate assessments of coastal erosion risks, enhanced disaster prediction, and the formulation of sustainable coastal engineering solutions [20–22].

Previous studies have extensively investigated the breaking characteristics of calcareous sand [23–26]. For instance, Coop [27] and Atkinson [28] comparatively examined the mechanical behaviors of calcareous sand with diverse cementation degrees, identifying particle breakage as a critical factor related to the high compressibility of calcareous sand. Kong and Fonseca [29] conducted confined compression tests on calcareous sand composed of shells, analyzed the evolution of particle morphology and coordination number during the compression process, and discussed the effects of particle morphology and fabric on interparticle relative motion. Wang et al. [30] concluded that the particle crushing strength of calcareous sand tends to decrease as the particle shape shifts from bulky to elongated and to flaky. Suescun-Florez et al. [31] tested the damage to calcareous sand during the compression phase, identifying that the effect of particle coordination number was greater than that of internal defects in particle breaking. Wang et al. [32] demonstrated that the compression modulus of calcareous silt decreased with decreasing compactness or increasing water content. By conducting triaxial shear tests on calcareous sand under different axial strains, Wang et al. [33] concluded that the particle breakage quantity of calcareous sand increased at a gradually decreasing rate with increasing axial strain and continued to increase even after reaching peak deviatoric stress. Moreover, over the past few decades, researchers have explored the mechanical characteristics and particle breakage evolution of coral sand using ring shearing tests [34], alongside triaxial tests [35–37] and model experiments [38,39]. However, changes in experimental methods have not resulted in a comprehensive understanding of the calcareous sand breakage mechanism.

Currently, the forefront of research on calcareous sand fragmentation predominantly centers on examining the evolution of single-particle test breaking modes with consideration of probability theory, as well as exploring the correlation between plastic work and particle breakage, along with the development of a novel estimation formulation for soil elastic modulus [40,41]. Nevertheless, there is inadequate research on the contact mode between calcareous sand particles and the evolution of the breakdown process under different influencing factors. Notably, existing studies predominantly center on the destruction of desiccated calcareous sand featuring uniform particle dimensions, mainly emphasizing relative density [42,43]. However, the South China Sea encompasses not only a substantial quantity of calcareous sand inclines but also considerable deposits of such sand below sea level. Hence, the processes governing the disruption of both dry and saturated sand directly influence the likelihood of coastal erosion. Additionally, given the extensive engineering infrastructure within the reefs of the South China Sea, it becomes imperative to evaluate the influence of loads and their associated loading trajectories.

The findings of this research substantially contribute to the formulation of more effective environmental protection measures, providing a scientific foundation for safeguarding ecological systems along coastlines. In this study, a series of lateral compression tests on full-grain-sized calcareous sand in the South China Sea were conducted to investigate the influence of relative density, loads, dry or wet states, and loading modes on the fragmen-

tation characteristics and compression properties of calcareous sand. The objective was to maximize the range of each parameter to obtain all responses to the breaking pattern of calcareous sand particles under individual factor variations. Moreover, a proposal was made to analyze the entire evolution pattern of particle crushing by combining the relative breakage rate with fractal dimensions. By delving into the mechanisms of particle cracking, this study offers more accurate theoretical guidance, enhancing the precision and reliability of predicting coastal erosion risks.

2. Materials and Methods

2.1. Test Material

The test material employed in this study consists of calcareous sand sourced from the Xisha Islands in the South China Sea. The diameter of the calcareous sand particles was less than 2 mm, covering the complete range of sand diameters. Figure 1 depicts the distribution curve and presents SEM and camera-generated images of the sand particles following the Standard for Geotechnical Testing Method (GB/T 50123-2019) [44]. These particles were primarily composed of fragments of reef limestone, shell, and coral, displaying a noticeable presence of densely distributed pores on their surfaces.

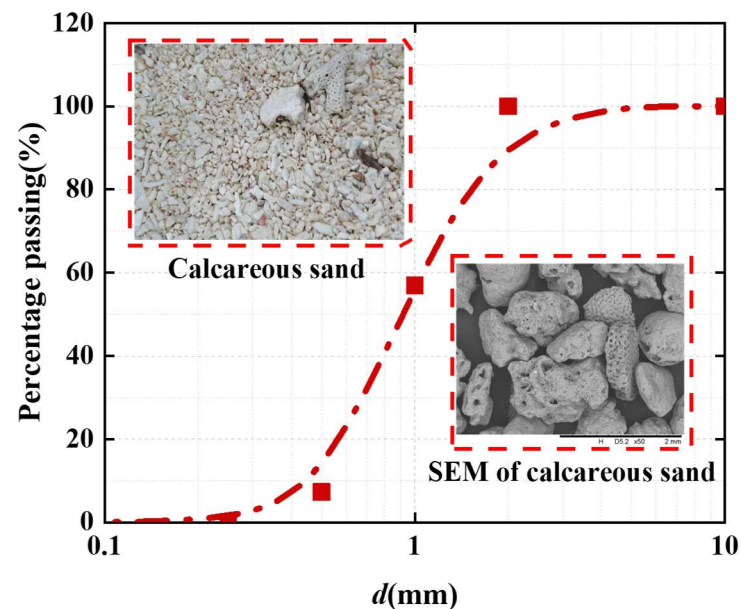


Figure 1. Particle size distribution curve, SEM, and camera photo of calcareous sand.

Table 1 presents the physical characteristics and gradation parameters of the calcareous sand, which were tested based on the Standard for Geotechnical Testing Method (GB/T 50123-2019). The maximum void ratio (e_{\max}) was found to be 1.344, while the minimum void ratio (e_{\min}) was determined to be 1.094. The specific gravity (G_s) was measured at 2.81. Additionally, the non-uniform coefficient (C_u) was determined to be 2.04, indicating a uniform distribution of particles within the sample, as it falls below the threshold of 5.00. The curvature coefficient (C_c) was calculated to be 0.953, suggesting a deficiency of particles between the d_{30} and d_{60} ranges. Due to its failure to meet the criteria of $C_u \geq 5$ and $1 \leq C_c \leq 3$ [45], the sand sample was categorized as poorly graded.

Table 1. The physical and gradation parameters of calcareous sand.

e_{\min}	e_{\max}	d_{10}/mm	d_{30}/mm	d_{60}/mm
1.094	1.344	0.446	0.675	1.072

2.2. Test Equipment

The test was performed using a WG-type single-lever medium-pressure oedometer manufactured by Nanjing Ningxi Soil Instrument Co., Ltd., Nanjing, China (Figure 2), according to the Standard for Geotechnical Testing Method (GB/T 50123-2019). This equipment consisted of three main components: a sample box, loading frame, and gauge. The test specimen had a height of 2 cm, an inner diameter of 6.18 cm, and a surface area of 30 cm².

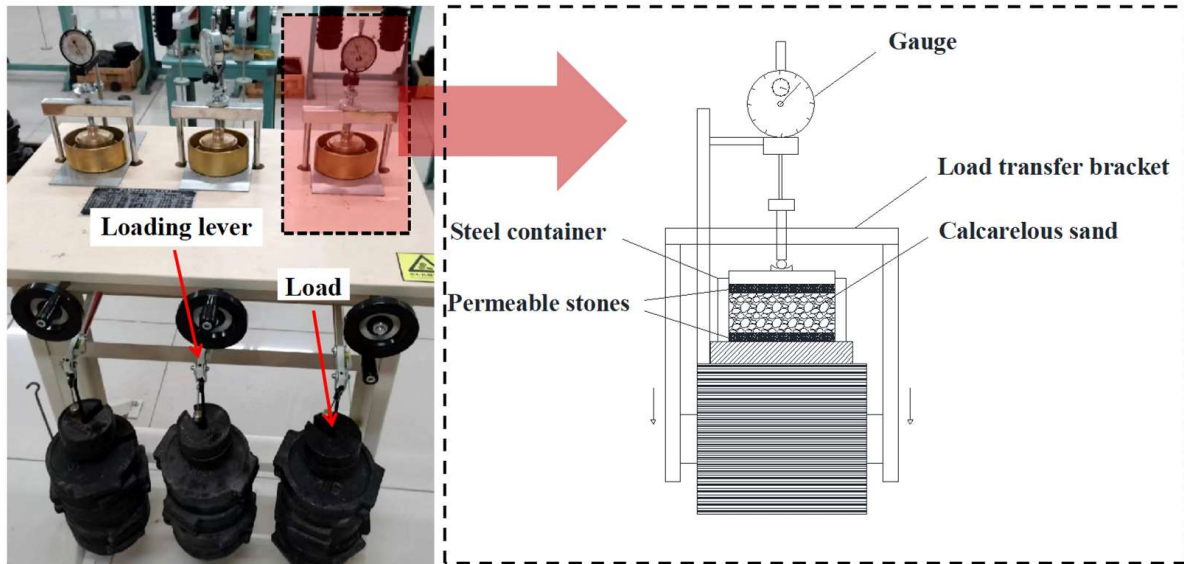


Figure 2. Confined compression equipment.

2.3. Test Scheme

This investigation aimed to analyze the confined-breaking properties of calcareous sand from the South China Sea under various conditions using α and B_r . Figure 3 depicts the experimental setup devised to examine the breaking characteristics of calcareous sands concerning different relative densities (D_r), ending vertical stresses (P_e), saturations (S_r), and loading modes (LM). The confined compression tests were conducted based on the parameters $D_r = 0.6$, $P_e = 1600$ kPa, and $S_r = 100\%$, employing a loading-unloading-reloading mode (Table 2). Prior to testing, the calcareous sand was washed with deionized water and air-dried to remove impurities that could potentially affect the experimental results. Each test group included three samples to ensure reproducibility and allow for parallel comparisons. The loading modes for vertical stress were designated as L1 and L2 in Table 2, with L1 and L2 representing the vertical stresses (P) varied in the following paths: 12.5 kPa \rightarrow 25 kPa \rightarrow 50 kPa \rightarrow 100 kPa \rightarrow 200 kPa \rightarrow 400 kPa \rightarrow 800 kPa \rightarrow 1600 kPa \rightarrow 800 kPa \rightarrow 400 kPa \rightarrow 200 kPa \rightarrow 100 kPa \rightarrow 50 kPa \rightarrow 25 kPa \rightarrow 12.5 kPa, and 12.5 kPa \rightarrow 25 kPa \rightarrow 50 kPa \rightarrow 100 kPa \rightarrow 200 kPa \rightarrow 400 kPa \rightarrow 800 kPa \rightarrow 1600 kPa, respectively. The D_r of the calcareous sands varied as 0.2, 0.4, 0.6, and 0.8, while the S_r of specimens were set at 0 and 100%, respectively, for a comparative analysis of the lateral mechanical response between dry sand and saturated sand [5]. Furthermore, the P_e was designated as 100 kPa, 200 kPa, 400 kPa, 800 kPa, and 1600 kPa to represent the different loading amplitudes corresponding to practical coastal engineering [46].

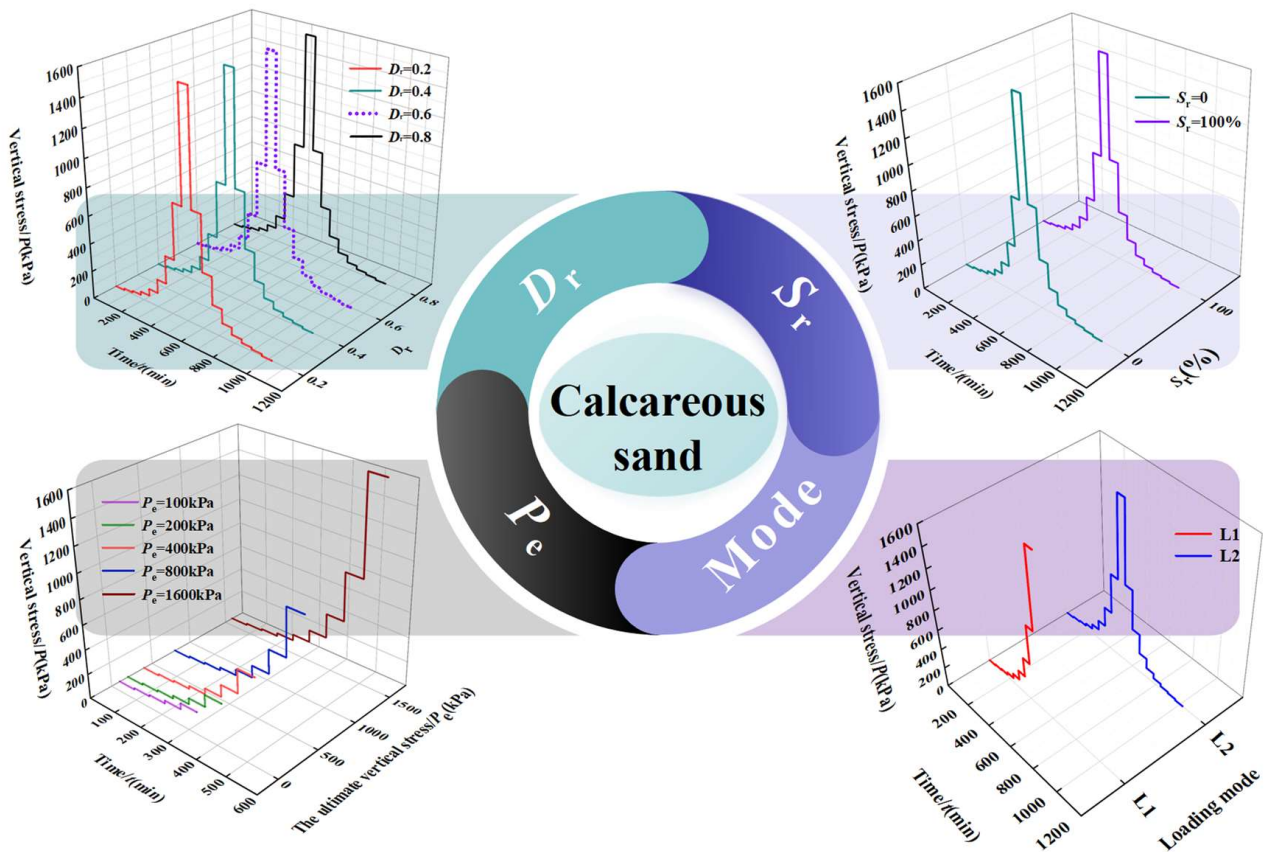


Figure 3. Loading process.

Table 2. Test scheme.

Test No.	D_r	LM	S_r	P_e (kPa)
T1	0.6	L2	100%	1600
T2	0.2	L2	100%	1600
T3	0.4	L2	100%	1600
T4	0.8	L2	100%	1600
T5	0.6	L1	100%	1600
T6	0.6	L2	0	1600
T7	0.6	L1	100%	100
T8	0.6	L1	100%	200
T9	0.6	L1	100%	400
T10	0.6	L1	100%	800

3. Results and Discussion

3.1. Compression Responses of Calcareous Sand

3.1.1. The Effect of Relative Density

Figures 4–6 depict the compression response of calcareous sands under different D_r with 100% of S_r , 1600 kPa of P_e , and following the L2 loading path. Figure 4 illustrates the correlation between void ratio (e) and $\lg P$ at various D_r . As shown in Figure 4a, a notable reduction in e was observed in calcareous sands during the initial loading phase across all groups. Additionally, in all groups, the e decreased as vertical stress increased during both the initial loading stage and the reloading stage. This decline can be attributed to two primary factors: the compression of interparticle voids due to particle positional adjustments and the occurrence of particle breakage, as demonstrated in the research conducted by Wang [47]. This finding holds significant implications for environmental engineering practice, particularly in the prevention of calcareous sand coastal erosion. By

understanding these mechanisms, more effective strategies would be devised for protecting calcareous sand coastlines, thereby reducing the environmental impact of calcareous sand erosion and sedimentation. During the unloading process, there is no significant rebound observed in the void ratio (e), indicating that the deformation is predominantly irreversible plastic deformation occurring during lateral compression of calcareous sand. This finding aligns with the experimental results obtained by Wang [48]. During the reloading phase, before reaching a 1600 kPa load, the e of calcareous sands across the four D_r grades surpassed that observed during the initial loading at equivalent loading levels. This disparity stems from the absence of new sand breakage during the reloading process until loads reached 1600 kPa. Following the initial loading stage, the recovered elastic deformation recurs during subsequent reloading. Subsequently, an increase in deformation was observed when P_e reached 1600 kPa, which might be attributed to the extrusion of pore water and the occurrence of new particle breakage.

Across all loading levels, a higher D_r corresponds to a lower initial void ratio (e_0), while this distinction among different groups gradually diminishes as the load increases. Furthermore, as shown in Figure 4b, at the initial loading stage above 200 kPa, all groups tend to have similar results, with the slope of the e - $\lg P$ curve remaining consistent. This slope stability originates from the initial reduction in e , which depends on the relative motion of particles. Therefore, a lower D_r provides greater movable space, resulting in a higher curve slope when the load is below 200 kPa. As the sample is gradually densified, limited space is available for particle movement. With increasing load, particle breakage occurs, leading to a renewed reduction in e and subsequently minimizing the impact of D_r .

At both the unloading and reloading stages, the relationship between e and $\lg P$ appears to exhibit a linear pattern, reminiscent of the reloading compression curve observed in clay, as depicted in Figure 4c,d.

Figure 5 depicts the correlation between compression stiffness (E_s) and P of calcareous sands under different D_r . During the initial loading stage, when P is below 200 kPa, the influence of D_r on the $E_s - P$ relationship behaves negligible. However, E_s exhibits an increase directly proportional to the rise in D_r as P exceeds 200 kPa. During the second loading phase, the compression stiffness (E_s) of the sands significantly surpasses the measurements observed during the initial loading stage under similar loading conditions, suggesting potential alterations in the internal particle structure following the initial loading. These alterations could be considered to induce a denser arrangement among the particles, resulting in higher stiffness during the subsequent loading phase. Moreover, post-initial loading changes, such as potential increases in internal particle friction or enhanced particle cohesion, could plausibly contribute to the observed heightened stiffness [48]. This indicates that preloading significantly contributes to the construction of a robust calcareous foundation. However, as the vertical stress (P) exceeds 800 kPa, a decline in E_s is observed due to the occurrence of new particle breakage within the calcareous sands. Additionally, an upward anomaly emerges on the $E_s - P$ curve during the reloading phase, attributed to the absorption of elastic deformation resulting from the unloading stage.

Figure 6 illustrates the correlation between the compression index (C_c) and vertical stress (P). During the initial loading phase, the C_c of the sand within the $D_r = 0.2$ group initially behaves in a decreasing direction, followed by an increase, and then exhibits a continuously increasing trend. This deviation markedly behaves differently from the outcomes observed in the remaining test groups, and this discrepancy could be attributed to the presence of substantial voids within the $D_r = 0.2$ specimen, resulting in a predominant point-to-point contact pattern among the granules. Similar results were observed by Shen et al. [46]. Consequently, a considerable allowance for particle movement could be considered to exist in the case of $D_r = 0.2$. With the development of the compaction of the specimen under continuous loading, the C_c behaved correspondingly in a decreasing direction. When P exceeds 25 kPa, most of the movable space within the $D_r = 0.2$ group has been compressed. Subsequently, the C_c exhibits a consistent increasing trend with the progressive increase in loading, mirroring the behavior observed in the other test groups. In

contrast, the C_c of other test groups ($D_r = 0.4, 0.6, 0.8$) always exhibits an incremental trend with the increase of P shown in Figure 6a, which can be attributed to the fact that they lack sufficient spaces to facilitate their particle movements under low stress conditions. This trend signifies the restricted motion of particles within the denser conditions, instigating an increase in C_c as stress intensified.

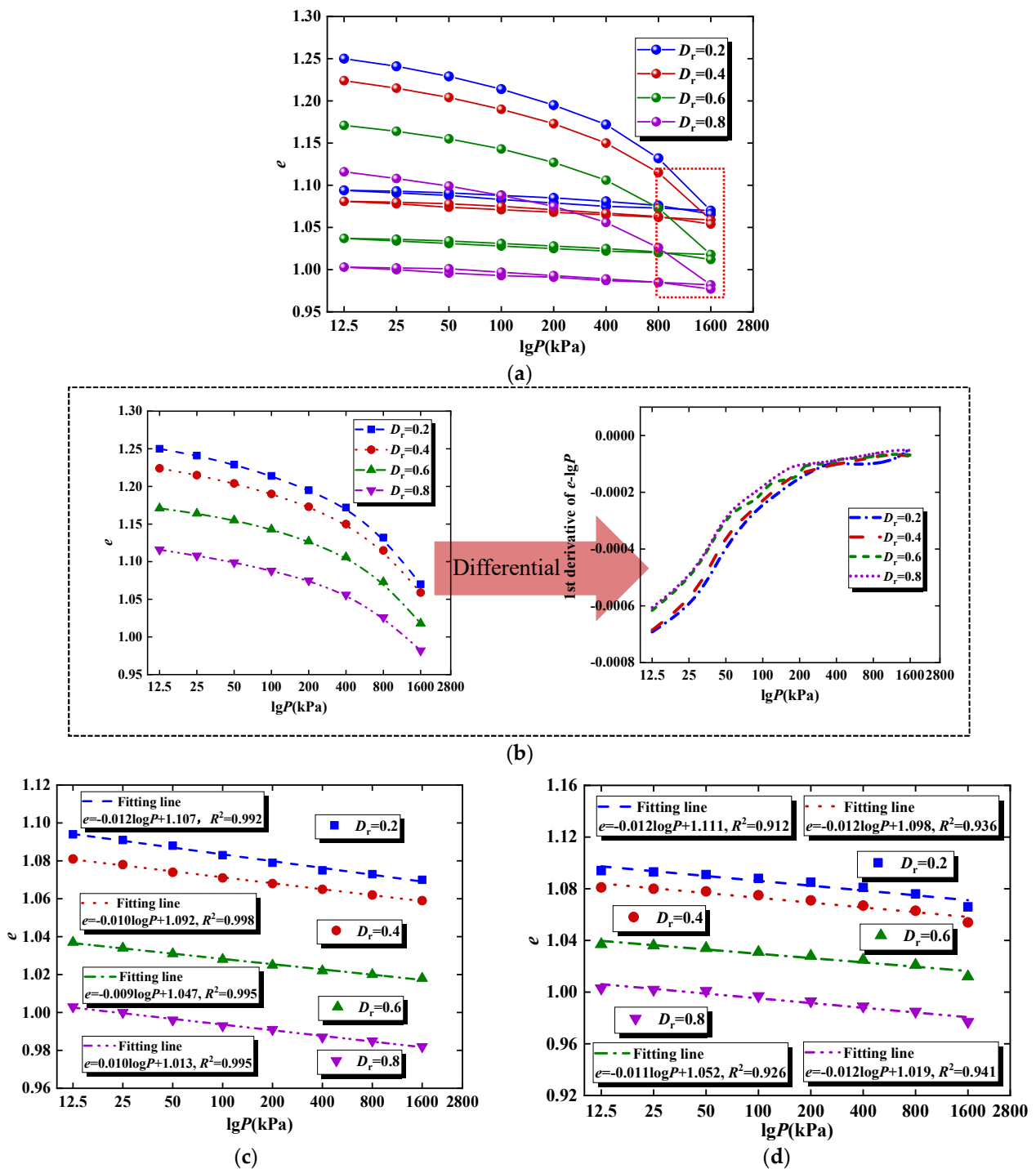


Figure 4. The $e-\lg P$ curves of calcareous sand under different D_r for (a) loading-unloading-reloading; (b) the first loading; (c) unloading; and (d) reloading.

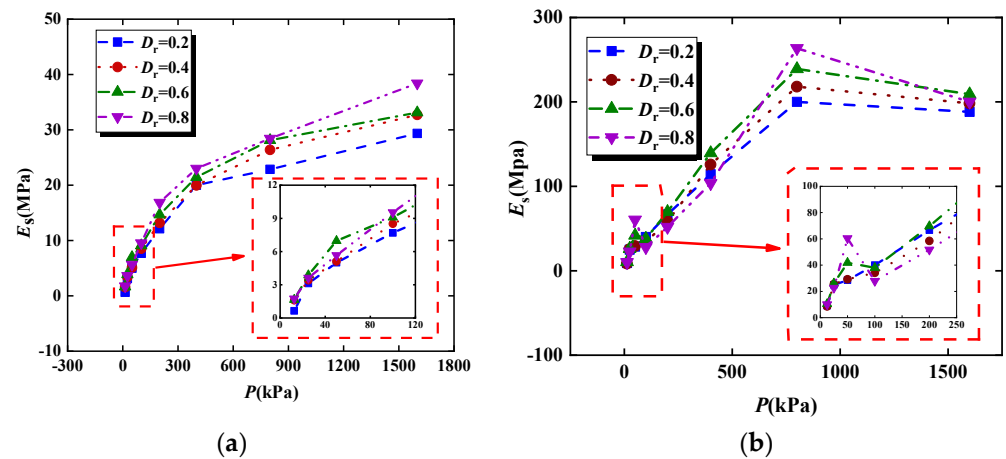


Figure 5. The $E_s - P$ curve of calcareous sand under different D_r at (a) the first loading and (b) the second loading.

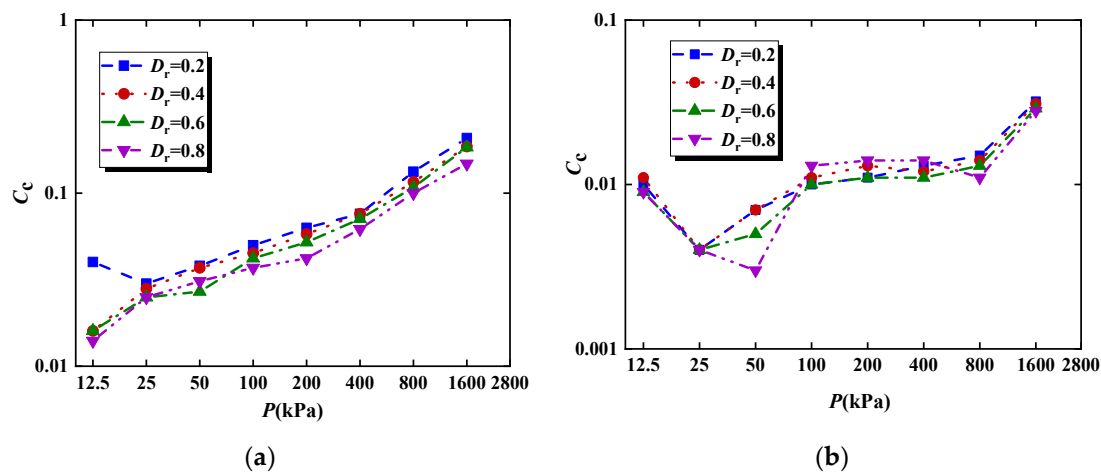


Figure 6. The $C_c - P$ curve of calcareous sand under different D_r at (a) the first loading and (b) the second loading.

During the reloading phase depicted in Figure 6b, the C_c of each group generally decreases compared to the measurements observed during the initial loading. Notably, the C_c initially declines and then increases as P ranges from 12.5 kPa to 50 kPa. This behavior can be attributed to the absorption of either partial or complete elastic deformation recovered from the unloading stage, as also evidenced in Figure 5b. Subsequently, all groups exhibit a phase of stability until P reaches 800 kPa. Beyond this point, the expulsion of water stored in the fine voids of the specimen occurs, followed by new particle breakage as P reaches 1600 kPa, leading to an increase in C_c , consistent with that displayed in Figure 5b.

3.1.2. Saturation Degree

Figures 7–9 illustrate the compression response of calcareous sand subjected to different S_r at $D_r = 0.6$ and $P_e = 1600$ kPa, following a repeated loading path of L2. Specifically, Figure 7 depicts the $e - \lg P$ curve for calcareous sand across different S_r . The e within the $S_r = 0$ group exceeds that observed in the $S_r = 100\%$ group across all loading grades. Conversely, while the sands within the $S_r = 100\%$ group exhibit lesser amplitude compared to $S_r = 0$ during the second loading stage, this disparity could be attributed to distinct behaviors at the initial loading. During the first loading, the water acts as a lubricant for the sand particles within the $S_r = 0$ group, inducing larger deformations. Yet, during the subsequent loading phase, substantial particle breakages occur in the calcareous sand, resulting in more compact inter-particle contact and finer void spaces. Consequently, nu-

merous semi-closed small pores are developed, yielding the accumulation of excess pore water pressure. This phenomenon impedes the decrease in e , accounting for the attenuated amplitude observed in the $S_r = 100\%$ group during the second loading stage.

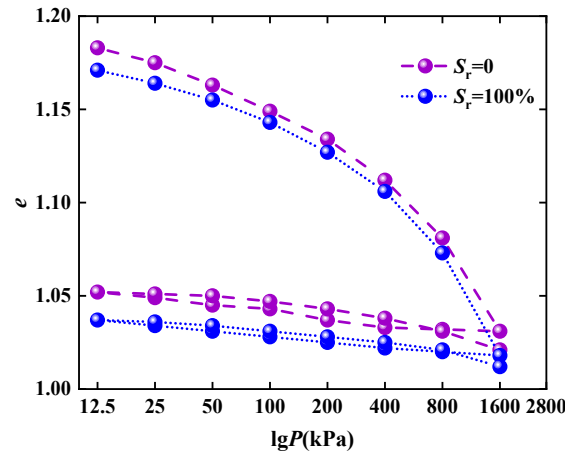


Figure 7. The e - $\lg P$ curve of calcareous sand under different S_r .

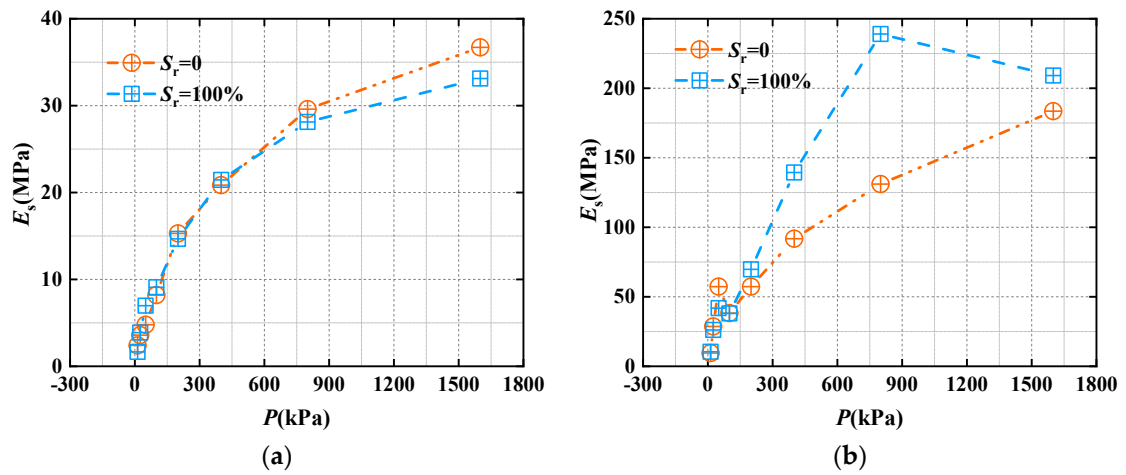


Figure 8. The $E_s - P$ curve of calcareous sand under different S_r at (a) the first loading and (b) the second loading.

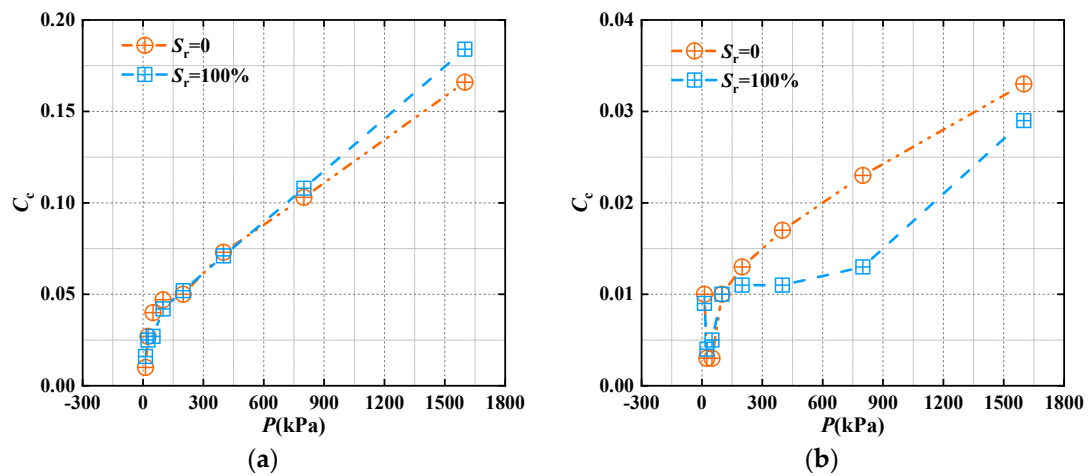


Figure 9. The $C_c - P$ curve of calcareous sand under different S_r at (a) the first loading and (b) the second loading.

Figure 8 illustrates the correlation between E_s and P across different S_r . Initially, at the onset of the first loading process, minimal variation existed in E_s between the two groups until P approached 800 kPa. Subsequently, a widening disparity in E_s becomes evident, prominently favoring the $S_r = 0$ group. This discrepancy could be attributed to the lubricative effect of water on sand particles as compaction occurs, thereby reducing the specimen's modulus.

During the reloading stage, a distinct disparity emerges, indicating a higher E_s for $S_r = 100\%$ compared to $S_r = 0$. This divergence stems from the substantial breakage induced by the initial loading, resulting in the formation of numerous semi-closed voids. The presence of these voids hinders the dissipation of water pore pressure, culminating in its accumulation. As P exceeded 800 kPa, the expulsion of water and subsequent deeper contraction of the specimen could lead to a decrease in E_s , as shown in Figure 8b.

Figure 9 illustrates the compression-load ($C_c - P$) curve depicting the behavior of calcareous sand under varying stress ratios (S_r). The change in C_c between the two loading stages exhibits a significant difference. Initially, during the primary loading phase, both groups showed an increase in C_c with the escalating load. However, the disparity between the two groups becomes apparent only after surpassing a threshold pressure (P) exceeding 800 kPa. The group with $S_r = 100\%$ demonstrates a higher C_c compared to $S_r = 0$, which could be attributed to the lubricating effect of water. Conversely, during the reloading stage, as P increased from 12.5 kPa to 100 kPa, both groups initially experienced a decrease in C_c , followed by an increase. This trend is likely attributed to the absorption of partial or complete elastic deformation recovered post-unloading. Subsequently, for the $S_r = 100\%$ group, C_c behaves steadily in increase with the rising load, whereas, for the $S_r = 0$ group, the variation in C_c remains stable as P increased from 100 kPa to 800 kPa due to the accumulation of water pore pressure. The water within the fine voids of the specimen behaves uncompressed until P reaches 1600 kPa, where a subsequent increase in C_c is observed.

3.2. Particle Breakage Responses of Calcareous Sand

3.2.1. Quantitative Assessment of Particle Breakage

Various indicators that characterize particle crushing have been documented in existing literature, encompassing parameters derived from individual particle size, gradation parameters, soil surface area, and gradation evolution [49–52]. However, these parameters often only capture changes in specified particle size or partial particles during the crushing process, or they merely demonstrate the overall amount of fragmentation after the experiment, leading to a biased and incomplete representation. Moreover, these indicators frequently encounter challenges in comprehensively investigating the intricate particle-breaking process and the comprehensive degree of particle crushing. Consequently, the relative breakage index (B_r) [53] and the fractal dimension (α) [54,55] have been favored for investigating the particle-breaking behavior of cohesionless soil.

1. Relative breakage index

Hardin's proposition [53] centered on the potential for particle breakage, which exhibited a close correlation with particle size (d). He introduced the concept of breaking potential in the overall gradation curve. Hardin suggested that particles smaller than 0.075 mm ceased to undergo further breakage, lacking the potential to generate additional breakage energy. Conversely, particles larger than 0.075 mm theoretically possessed the capacity for breakage, thereby engendering breakage potential. Hardin defined the breaking potential, B_t , as the area enclosed between the initial particle size distribution curve, the upper limit of silt particle diameter at 0.075 mm, and the particle size distribution curve post-test. Consequently, Hardin introduced a novel metric to quantify particle breakage, denoted as the relative breakage rate B_r , illustrated in Figure 10 as follows:

$$B_r = \frac{B_t}{B_p} \quad (1)$$

where the total breakage, B_t , represents the area between the initial particle size distribution curve and the current grading curve, denoted as $Area_{dbcd}$; B_p represents the breakage potential, that is, the area between the initial particle size distribution curve and the boundary at $d = 0.075$ mm, denoted as $Area_{abca}$.

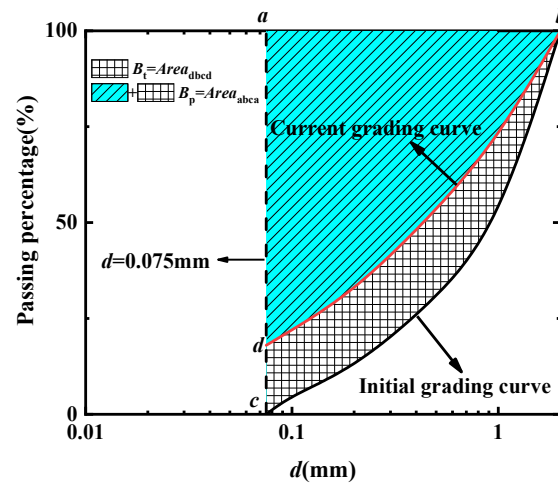


Figure 10. Definition of particle breakage index.

While the utilization of B_t as an indicator effectively assessed the overall extent of particle breakage, it lacked utility in discerning specific breaking modes prevalent during the compression process, such as abrasion, crushing, and cracking [56,57].

2. Fractal dimension

The fractal theory had been widely employed to describe the irregularity and self-similarity of objects. Researchers utilized the fractal theory to analyze the particle size distribution within granular geotechnical materials, postulating that these materials conform to this principle [54,55]:

$$f(d) = \left(\frac{d}{d_{\max}} \right)^{3-\alpha} \quad (2)$$

where $f(d)$ represents the mass fraction of particles $< d$ in size; d_{\max} represents the upper limit of particle size; and α represents the fractal dimension. Performing logarithmic processing on Equation (3) yields:

$$\alpha = 3 - \frac{\lg f(d)}{\lg \left(\frac{d}{d_{\max}} \right)} \quad (3)$$

Based on Equation (3), the variation trend of α displays a negative correlation with the alteration of $\frac{\lg f(d)}{\lg \left(\frac{d}{d_{\max}} \right)}$, as depicted in Figure 11. In the $\lg f(d) - \lg \left(\frac{d}{d_{\max}} \right)$ coordinate system, an increased slope indicates a transition from smaller to larger particles, accompanied by a decrease in α , denoted as $\Delta\alpha < 0$. Conversely, a decreased slope indicates a transition from larger to smaller particles, coupled with an increase α , that is, $\Delta\alpha > 0$.

Assessing particle breakage modes under distinct test schemes based on the value of $\Delta\alpha$ is feasible. However, relying solely on $\Delta\alpha$ may not accurately determine the overall degree of particle breakage [58,59]. Consequently, a comprehensive evaluation of particle breakage necessitates the integration of B_t and $\Delta\alpha$, believed to offer essential and reliable potential for precisely assessing the particle breakage behavior of calcareous sand.

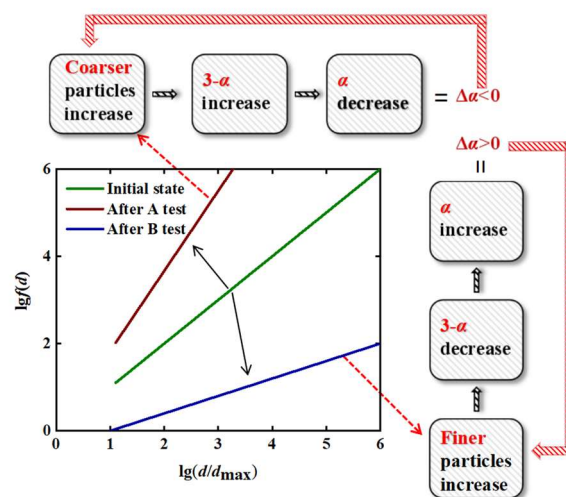


Figure 11. The relationship between $\Delta\alpha$ and the ratio of coarser particles to finer particles.

3.2.2. The Effect of Relative Density

Figures 12–14 depict the influence of D_r on the response of calcareous sands to breakage under conditions of $P_e = 1600$ kPa, $S_r = 100\%$, and following L2. In Figure 12, the distribution curves of calcareous sands at different D_r are presented, highlighting five distinct points. The distribution curve of loose sand ($D_r = 0.2$) occupies the uppermost position, indicating comprehensive particle breakage across all size ranges of calcareous sands. This can be attributed to the prevalent point-to-point contact mode among particles when $D_r = 0.2$. In contrast to the point-to-face and face-to-face contact modes, the point-to-point contact mode results in a smaller inter-particle contact area, leading to increased contact stress and, consequently, more pronounced fragmentation, which is consistent with the experimental results of Shen [46]. Comparatively, medium-dense and dense sands exhibit more breakage in looser sands with minor fluctuations, predominantly influenced by the morphology of the calcareous sands.

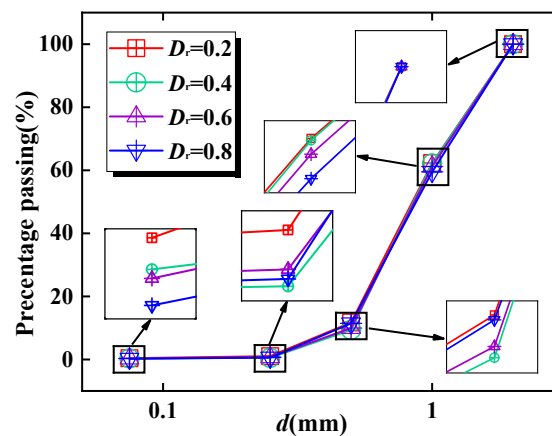


Figure 12. Particle size distribution curve of calcareous sands under different D_r .

In Figure 13, the percentile diameters (PD) of calcareous sands under various D_r are depicted, including d_{10} , d_{30} , d_{50} , and d_{60} . It can be observed from the graph that the smaller the D_r , the more pronounced the fragmentation of calcareous sands. Additionally, the influence of D_r on the fragmentation of calcareous sands primarily focuses on smaller particle sizes. As shown in the graph, when $D_r = 0.2$, d_{10} , d_{30} , and d_{50} are all the smallest. However, d_{60} is the same as $D_r = 0.4$ at 1 mm. Additionally, for medium-dense sands, the influence of relative density is less pronounced, as the PD for $D_r = 0.4$ and $D_r = 0.6$ are the same for all parameters except for d_{60} , where $D_r = 0.6$ exhibits a slightly higher value of

0.023 compared to $D_r = 0.4$. For dense sands, specimens with $D_r = 0.8$ demonstrate the least overall degree of fragmentation.

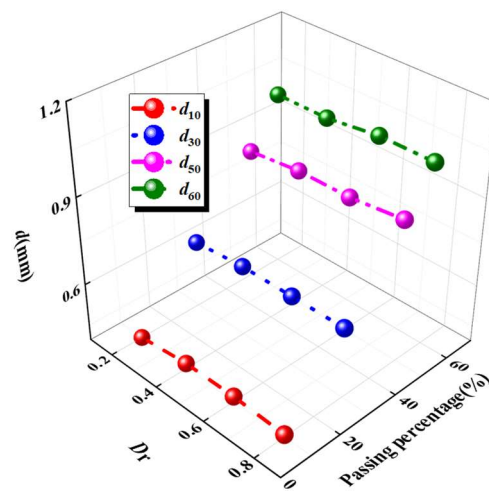


Figure 13. The PD of calcareous sands under different D_r .

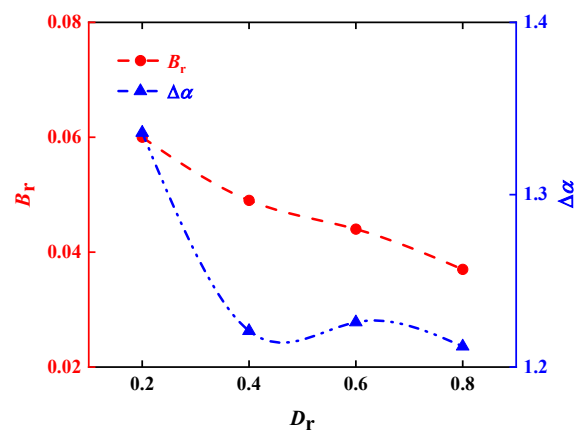


Figure 14. The relationship of B_r and $\Delta\alpha$ of calcareous sands under different D_r .

Figure 14 presents the correlation between B_r and $\Delta\alpha$ of calcareous sands at varying D_r . It is discernible that the overall degrees of breakage gradually diminish with the increases in D_r . This trend aligns with the reduction in contact stress attributed to the elevated D_r . This indicates that analyzing the fragmentation of calcareous sands solely based on the pattern of PD in Figure 13 is highly limited, and PD alone cannot be used to analyze the overall fragmentation of calcareous sands. Nevertheless, the alteration pattern of $\Delta\alpha$ varies distinctly among the groups. For the group of $D_r = 0.2$, $\Delta\alpha$ surpasses 0.06, indicating the dominance of crush and crack propagation as the primary modes of particle breakage within this group. In contrast, additional groups display $\Delta\alpha$ within the range of 0.02 to 0.03, indicative of an absence of pronounced discrepancies. This observation underscores that, except for the group with $D_r = 0.2$, abrasion emerges as the primary mode of particle breakage. Despite observed variations in the degree of particle breakage among the $D_r = 0.4$, 0.6, and 0.8 groups based on B_r , abrasion continues to represent the prevailing mechanism in these groups.

3.2.3. The Effect of Ending Load

Figures 15–17 illustrate the response of calcareous sands to breakage under various ending loading (P_e) conditions with $D_r = 0.6$, $S_r = 100\%$, and following L1. As shown in Figure 15, the particle breakage level exhibits an incremental trend with increasing P_e . Distinguishedly, for particles over 1 mm in size, the difference in particle breakage is limited

for P_e less than 400 kPa. This implies that particle breakage predominantly originates from the intermediate-sized particles ($d < 1$ mm) with the progressive increase in loading.

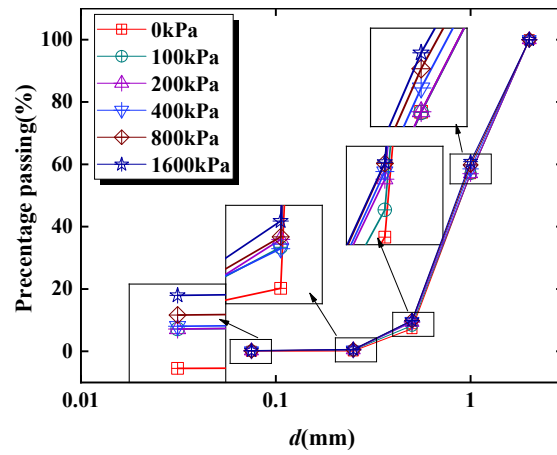


Figure 15. Particle size distribution curve of calcareous sands under different P_e .

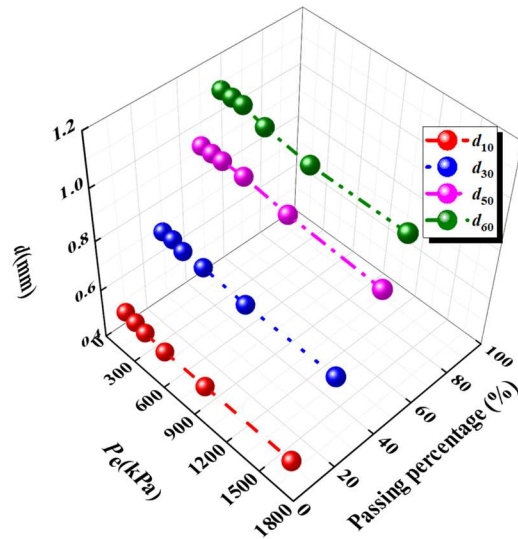


Figure 16. The PD of calcareous sands under different P_e .

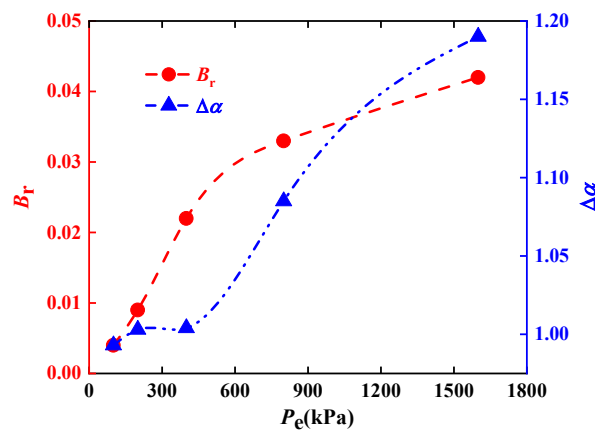


Figure 17. The relationship between B_r , $\Delta\alpha$ of calcareous sands and P_e .

As depicted in Figure 16, when P_e is 100 kPa, only d_{10} experiences a marginal decrease of 0.01, while the remaining PD remain unaffected. When P_e reaches 400 kPa, there is a

notable decrease in d_{60} , from 1.071 mm to 1.046 mm, consistent with the trend portrayed in Figure 15. This indicates an increase in the particle size susceptible to fragmentation. Additionally, there is no distinct variation observed in the PD of all characteristic particle sizes between $P_e = 800$ kPa and $P_e = 1600$ kPa. Notably, the fragmentation observed in fine-grained calcareous sand under these loads, as indicated by the changing pattern of d_{10} , signifies an amplified mechanical susceptibility of the fine-grained calcareous sand to externally induced forces. Importantly, when P_e is less than 400 kPa, only fine-grained calcareous sand experiences fragmentation. Specifically, as P_e increases while remaining below 400 kPa, both d_{10} and d_{30} decrease, while other PD remains unchanged. However, Figures 15 and 16 fail to comprehensively illustrate the fragmentation patterns of particles ranging from 1 mm to 2 mm in diameter.

In Figure 17, a notable increase in B_r is observed as P_e escalates from 200 kPa to 400 kPa, which is consistent with the patterns observed in the experiments conducted by Xue [23]. This indicates that significant breakage occurs under the condition of $P_e = 400$ kPa. Meanwhile, the corresponding $\Delta\alpha$ at this stage is minimal, suggesting minor breakage in larger-sized particles (particle diameter greater than 1.0 mm). Hence, the breakage observed in calcareous sand primarily focuses on the fracture of smaller particles and the erosion of larger particles. When P_e reaches 800 kPa, significant fragmentation occurs in larger-sized calcareous sand particles, and the corresponding $\Delta\alpha$ at this stage also significantly increases. Figure 17 compensates for the shortcomings of Figures 15 and 16, allowing for the observation of both the overall degree of sample fragmentation and the fragmentation patterns of particles within various size ranges.

3.2.4. The Effect of the Loading Path

Figures 18–20 illustrate the breakage response of calcareous sands under monotonic loading paths and repeated loading paths (denoted as L1 and L2 shown in Table 1), both maintaining $D_r = 0.6$, $S_r = 100\%$, and $P_e = 1600$ kPa.

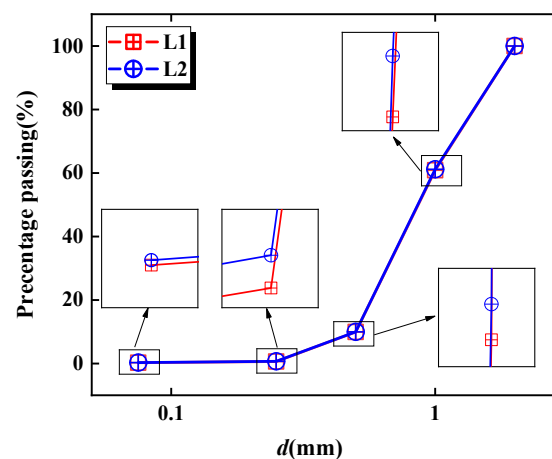


Figure 18. Particle size distribution curve of calcareous sands under different LM.

As depicted in Figure 18, the influence of repeated loading on the breakage of calcareous sands was minimal. Results obtained under L2 show only slightly higher values compared to those under L1, with differences considered negligible. The primary breakage of calcareous sand could be observed during the initial loading stage, leading to the formation of a stable particle contact mode. Consequently, negligible breakage is observed during subsequent repeated loading under the same loading amplitude, with only minor abrasion observed.

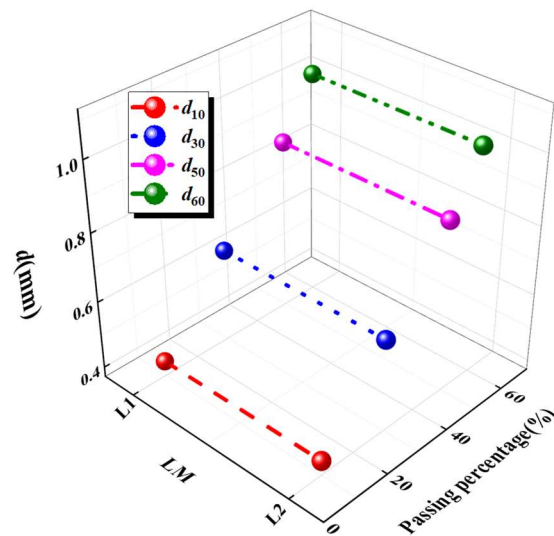


Figure 19. The PD of calcareous sands under different LM.

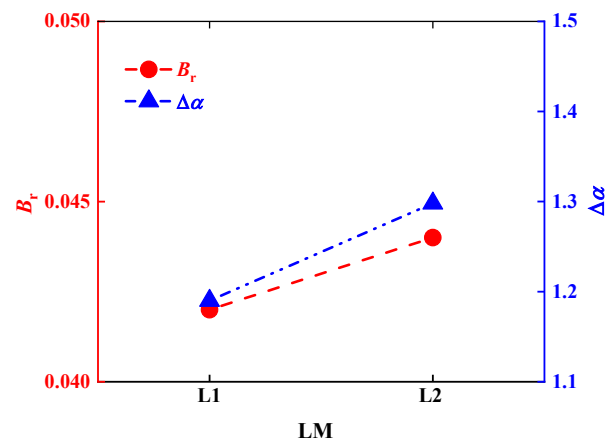


Figure 20. The relationship between B_r , $\Delta\alpha$ of calcareous sands and LM.

As shown in Figure 19, the PDs of d_{10} , d_{30} , d_{50} , and d_{60} exhibit considerable proximity. There is minimal evidence of breakage upon the second loading, consistently aligning with the outcomes observed in Figure 18. Similarly, as depicted in Figure 20, a similar trend is observed, indicating a minor degree of fragmentation in smaller sands upon the second loading.

3.2.5. The Effect of Saturation Degree

Figures 21–23 delineate the breakage response of calcareous sands under varying degrees of saturation (S_r) with a D_r of 0.6, S_r of 100%, and following the L2 loading path.

As depicted in Figure 21, dried calcareous sands exhibit increased susceptibility to breakage due to the significant influence of interparticle friction. In contrast, saturated calcareous sands, facilitated by water lubrication, experience a notable reduction in intergranular friction. Moreover, a higher proportion of fine grains is observed in the $S_r = 100\%$ group. This is primarily attributed to the lubricating effect of water, which reduces the friction between particles and alters their relative motions and interactions. Consequently, the stability of the initial calcium sand particle framework is reduced, and the relative sliding space between particles increases. Under vertical loading, the increased relative sliding space may render weak points or vulnerable areas within particles more susceptible to external forces. These vulnerabilities typically reside at particle edges or within localized weak zones of the particle structure. Owing to this lubricating effect, particle movements may induce additional stresses at particle edges or weak points, resulting in abrasion or

minor fragmentation along particle edges. Hence, the lubricating action of pore water could intensify the movement at particle edges or weak areas and instigate minor abrasion or cracking at these specific locations.

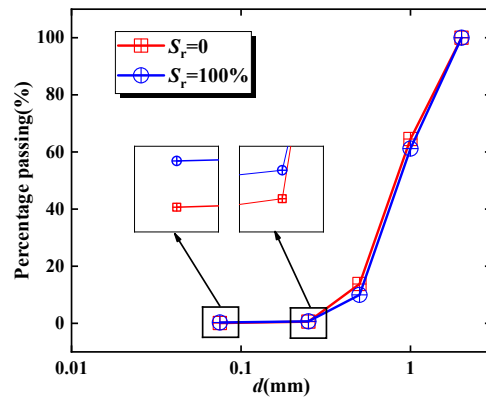


Figure 21. Particle size distribution curve of calcareous sands under different S_r .

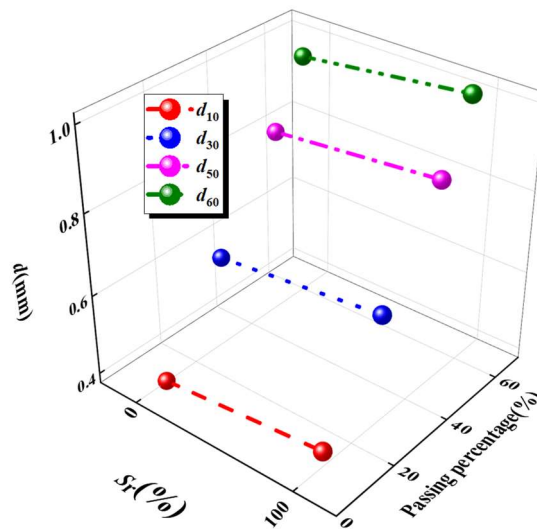


Figure 22. The PD of calcareous sands under different S_r .

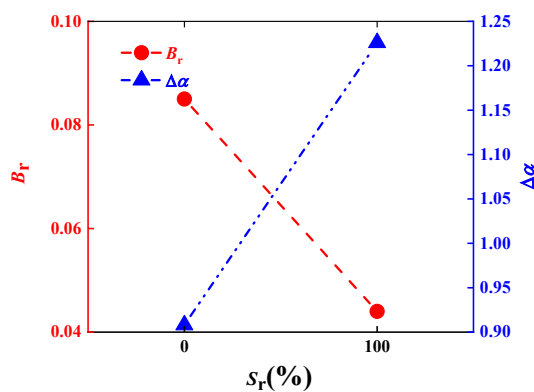


Figure 23. The relationship between B_r , $\Delta\alpha$ of calcareous sands and S_r .

Figure 22 demonstrates a notable distinction in percentile diameters (PD) for each characteristic particle size between $S_r = 0$ and $S_r = 100\%$. Furthermore, the PD associated with $S_r = 100\%$ consistently surpasses that of $S_r = 0$ at equivalent passing percentages. For $S_r = 0$, the particle size distribution is characterized by $d_{10} = 0.377$, $d_{30} = 0.601$, $d_{50} = 0.832$,

and $d_{60} = 0.977$. In contrast, for $S_r = 100\%$, the corresponding results are $d_{10} = 0.415$, $d_{30} = 0.644$, $d_{50} = 0.87$, and $d_{60} = 1.023$. Consequently, the extent of specimen breakage in $S_r = 0$ is more pronounced than that observed in $S_r = 100\%$. Moreover, combining with Figure 21, the proportion of debris after the abrasion of specimens with $S_r = 100\%$ is found to be less than 10%. This analysis provides insight into the test results, such as the lower d_{10} value for $S_r = 0$ compared to that for $S_r = 100\%$.

Figure 23 depicts a stark contrast in patterns between B_r and $\Delta\alpha$. While the B_r for $S_r = 0$ remains larger, the $\Delta\alpha$ behaves smaller compared to that for $S_r = 100\%$. This indicates that saturated sands generate a greater total quantity of fine particles post-compression, despite dried calcareous sands exhibiting higher crushing quantities.

4. Conclusions

This study aimed to quantitatively evaluate the compression and particle fragmentation of calcareous sand in the South China Sea under varying conditions, including relative density, saturation, loads, and loading paths. Subsequently, a series of confined compression tests were conducted on the widely distributed calcareous sand, and the associated particle-breaking mechanisms of calcareous sands under diverse testing conditions were investigated using relative breakage ratio and fractal dimension as assessment parameters. The principal conclusions derived from this study could be summarized as follows:

1. Increasing relative density induces a transition in particle contact patterns from predominantly point-to-point contact to face-to-face contact, resulting in reduced inter-particle contact stress and overall fragmentation. The influence of relative density on sample deformation is particularly pronounced under initial loading conditions below 200 kPa. Variations in sample deformation under different relative densities primarily stem from differences in the initial available void space within the calcareous sand.
2. Increasing loads intensified particle breakage, particularly with finer particles. Noticeable breakage of particles with a diameter close to 1 mm occurred only after loads surpassed 200 kPa, while cracking of all larger particles was observed after loads exceeded 400 kPa.
3. Loading paths showed minimal impact on particle crushing. During the second loading phase, pore ratios under various load levels surpassed those observed during the initial loading, leading to new fragmentation only at loads reaching 1600 kPa, accompanied by the expulsion of pore water and dissipation of pore pressure.
4. The lubricating effect of water could reduce the inter-particle friction, thereby diminishing overall breakage. However, increasing relative sliding could intensify stress points at particle edges, resulting in localized abrasion. Although this did not affect the main structure, it led to an increased content of finer particles. The influence of pore water pressure was primarily manifested when numerous semi-enclosed pores existed within the specimen during the second loading phase.
5. Currently, our research on calcareous sand breakage is limited to confined compression tests. However, erosion on calcareous sand coastlines is largely caused by dynamic loads such as extreme wave loading and seismic activities. Therefore, the next phase of our research will investigate calcareous sand fragmentation characteristics under dynamic loading conditions, considering various influencing factors.

Author Contributions: Conceptualization, methodology, and writing-original draft preparation, J.Z.; data curation and software, Q.Z.; validation and investigation, H.Y. All authors have read and agreed to the published version of the manuscript.

Funding: This research was funded by the National Nature Science Foundation of China (Grant No. 51879133) and the Commonweal Project of Zhejiang Province (Grant No. LGG22E090002).

Institutional Review Board Statement: Not applicable.

Informed Consent Statement: Not applicable.

Data Availability Statement: The dataset is available from the corresponding author upon reasonable request.

Conflicts of Interest: The authors declare no conflicts of interest.

References

1. Li, L.; Beemer, R.; Iskander, M. Granulometry of two marine calcareous sands. *J. Geotech. Geoenviron. Eng.* **2021**, *147*, 04020171. [[CrossRef](#)]
2. Liu, L.; Yao, X.; Ji, Z.; Gao, H.; Wang, Z.; Shen, Z. Cyclic Behavior of Calcareous Sand from the South China Sea. *J. Mar. Sci. Eng.* **2021**, *9*, 1014. [[CrossRef](#)]
3. Yu, F. Characteristics of particle breakage of sand in triaxial shear. *Powder Technol.* **2017**, *320*, 656–667. [[CrossRef](#)]
4. Wang, X.; Wang, X.; Jin, Z.; Meng, Q.; Zhu, C.; Wang, R. Shear characteristics of calcareous gravelly soil. *Bull. Eng. Geol. Environ.* **2017**, *76*, 561–573. [[CrossRef](#)]
5. Wang, X.; Wang, X.; Shen, J.; Ding, H.; Wen, D.; Zhu, C.; Lv, S. Foundation filling performance of calcareous soil on coral reefs in the South China Sea. *Appl. Ocean Res.* **2022**, *129*, 103386. [[CrossRef](#)]
6. He, S.; Ding, Z.; Sun, Y.; Chen, W.; Xia, T. Cumulative deformations and particle breakage in calcareous sand subjected to drained high-cyclic loading: Experimental investigation. *Soil Dyn. Earthq. Eng.* **2022**, *161*, 107417. [[CrossRef](#)]
7. Shen, Y.; Zhu, Y.; Liu, H.; Li, A.; Ge, H. Macro-meso effects of gradation and particle morphology on the compressibility characteristics of calcareous sand. *Bull. Eng. Geol. Environ.* **2018**, *77*, 1047–1055. [[CrossRef](#)]
8. Wang, X.; Wu, Y.; Cui, J.; Zhu, C.; Wang, X. Shape characteristics of coral sand from the South China Sea. *J. Mar. Sci. Eng.* **2020**, *8*, 803. [[CrossRef](#)]
9. Zhu, C.; Chen, H.; Meng, Q.; Wang, R. Microscopic characterization of intrapore structures of calcareous sands. *Rock Soil Mech.* **2014**, *35*, 1831–1836. [[CrossRef](#)]
10. Ye, J.; Zhang, Z.; Shan, J. Statistics-based method for determination of drag coefficient for nonlinear porous flow in calcareous sand soil. *Bull. Eng. Geol. Environ.* **2019**, *78*, 3663–3670. [[CrossRef](#)]
11. Wu, Y.; Li, N.; Wang, X.; Cui, J.; Chen, Y.; Wu, Y.; Yamamoto, H. Experimental investigation on mechanical behavior and particle crushing of calcareous sand retrieved from South China Sea. *Eng. Geol.* **2021**, *280*, 105932. [[CrossRef](#)]
12. Lv, Y.; Li, X.; Fan, C.; Su, Y. Effects of internal pores on the mechanical properties of marine calcareous sand particles. *Acta Geotech.* **2021**, *16*, 3209–3228. [[CrossRef](#)]
13. Cooper, M.; Sorensen, K.; Freitas, T.; Georgoutsos, G. Particle breakage during shearing of a carbonate sand. *Géotechnique* **2004**, *54*, 157–163. [[CrossRef](#)]
14. Skaropoulou, A.; Kakali, G.; Tsivilis, S. Thaumasite form of sulfate attack in limestone cement concrete: The effect of cement composition, sand type and exposure temperature. *Constr. Build. Mater.* **2012**, *36*, 527–533. [[CrossRef](#)]
15. Flor-Blanco, G.; Bruschi, V.; Adrados, L.; Domínguez-Cuesta, M.; Gracia-Prieto, F.; Llana-Fúnez, S. Geomorphological evolution of the calcareous coastal cliffs in North Iberia (Asturias and Cantabria regions). *Estuar. Coast. Shelf Sci.* **2022**, *273*, 107913. [[CrossRef](#)]
16. Ortega, A.; Díaz, L.; Cueto, J. Assessment and management of coastal erosion in the marine protected area of the Rosario Island archipelago (Colombian Caribbean). *Ocean Coast. Manag.* **2023**, *239*, 106605. [[CrossRef](#)]
17. Zeng, H.; Yin, L.; Tang, C.; Zhu, C.; Cheng, Q.; Li, H.; Lv, C.; Shi, B. Tensile behavior of bio-cemented, fiber-reinforced calcareous sand from coastal zone. *Eng. Geol.* **2021**, *294*, 106390. [[CrossRef](#)]
18. Wang, S.; Huang, Y. Experimental study on the effect of particle breakage on the shear characteristics of large-displacement soil exposed to heat treatment. *Eng. Geol.* **2023**, *323*, 107219. [[CrossRef](#)]
19. Kosciuch, T.; Pilarczyk, J.; Hong, I.; Fritz, H.; Horton, B.; Rarai, A.; Harrison, M.; Jockley, F. Foraminifera reveal a shallow nearshore origin for overwash sediments deposited by Tropical Cyclone Pam in Vanuatu (South Pacific). *Mar. Geol.* **2018**, *396*, 171–185. [[CrossRef](#)]
20. Xiong, H.; Qiu, Y.; Liu, J.; Yin, Z.; Chen, X. Macro–microscopic mechanism of suffusion in calcareous sand under tidal fluctuations by coupled CFD-DEM. *Comput. Geotech.* **2023**, *162*, 105676. [[CrossRef](#)]
21. McDougall, C. Erosion and the beaches of Negril. *Ocean Coast. Manag.* **2017**, *148*, 204–213. [[CrossRef](#)]
22. Silva, A.; Leão, Z.; Kikuchi, R.; Costa, A.; Souza, J. Sedimentation in the coastal reefs of Abrolhos over the last decades. *Cont. Shelf Res.* **2013**, *70*, 159–167. [[CrossRef](#)]
23. Li, X.; Liu, J. One-dimensional compression feature and particle crushability behavior of dry calcareous sand considering fine-grained soil content and relative compaction. *Bull. Eng. Geol. Environ.* **2021**, *80*, 4049–4065. [[CrossRef](#)]
24. Li, X.; Liu, J.; Sun, Z. Impacts of organic matter and loading methods on one dimensional compression behavior of calcareous sand. *Mar. Georesour. Geotechnol.* **2021**, *40*, 1046–1059. [[CrossRef](#)]
25. Peng, Y.; Ding, X.; Zhang, Y.; Wang, C.; Wang, C. Evaluation of the particle breakage of calcareous sand based on the detailed probability of grain survival: An application of repeated low-energy impacts. *Soil Dyn. Earthq. Eng.* **2021**, *141*, 106497. [[CrossRef](#)]
26. Shen, J.; Wang, X.; Shan, Y.; Cui, J.; Chen, X.; Wang, X.; Zhu, C. Particle breakage and shape analysis of calcareous sand under consolidated-undrained triaxial shear. *Bull. Eng. Geol. Environ.* **2022**, *81*, 232. [[CrossRef](#)]
27. Coop, M. The mechanics of uncemented carbonate sands. *Géotechnique* **1990**, *40*, 607–626. [[CrossRef](#)]
28. Coop, M.; Atkinson, J. The mechanics of cemented carbonate sands. *Géotechnique* **1993**, *43*, 53–67. [[CrossRef](#)]
29. Kong, D.; Fonseca, J. On the kinematics of shelly carbonate sand using X-ray micro tomography. *Eng. Geol.* **2019**, *261*, 105268. [[CrossRef](#)]

30. Wan, T.; Ma, L.; Wang, M.; Li, Z.; Zhan, X.; Geng, H. Effects of particle shape on dynamic mechanical behaviours of coral sand under one-dimensional compression. *Eng. Geol.* **2022**, *304*, 106624. [[CrossRef](#)]
31. Suescun-Florez, E.; Iskander, M.; Bless, S. Evolution of particle damage of sand during axial compression via arrested tests. *Acta Geotech.* **2020**, *15*, 95–112. [[CrossRef](#)]
32. Wang, X.; Cui, J.; Wu, Y.; Zhu, C.; Wang, X. Mechanical properties of calcareous silts in a hydraulic fill island-reef. *Mar. Georesour. Geotechnol.* **2020**, *39*, 1–14. [[CrossRef](#)]
33. Wang, G.; Wang, Z.; Ye, Q.; Zha, J. Particle breakage evolution of coral sand using triaxial compression tests. *J. Rock Mech. Geotech.* **2021**, *13*, 321–334. [[CrossRef](#)]
34. Miao, G.; Airey, D. Breakage and ultimate states for a carbonate sand. *Géotechnique* **2013**, *63*, 1221–1229. [[CrossRef](#)]
35. Wei, H.; Liu, H.; Li, X.; Tao, Z.; Wu, Y.; Shen, J.; Yin, M. Effect of stress path on the mechanical properties of calcareous sand. *Undergr. Space* **2023**, *9*, 20–30. [[CrossRef](#)]
36. Shahnazari, H.; Rezvani, R. Effective parameters for the particle breakage of calcareous sands: An experimental study. *Eng. Geol.* **2013**, *159*, 98–105. [[CrossRef](#)]
37. Li, X.; Liu, J.; Nan, J. Prediction of dynamic pore water pressure for calcareous sand mixed with fine-grained soil under cyclic loading. *Soil Dyn. Earthq. Eng.* **2022**, *157*, 107276. [[CrossRef](#)]
38. Zhang, X.; Chen, Y.; Liu, H.; Zhang, Z.; Ding, X. Performance evaluation of a MICP-treated calcareous sandy foundation using shake table tests. *Soil Dyn. Earthq. Eng.* **2020**, *129*, 105959. [[CrossRef](#)]
39. Cao, D.; Shukla, S.; Yang, L.; Guo, C.; Wu, J.; Wang, F. Responses of calcareous sand foundations to variations of groundwater table and applied loads. *J. Rock Mech. Geotech. Eng.* **2022**, *14*, 1266–1279. [[CrossRef](#)]
40. Gao, R.; Ye, J. Mechanical behaviors of coral sand and relationship between particle breakage and plastic work. *Eng. Geol.* **2023**, *316*, 107063. [[CrossRef](#)]
41. Gao, R.; Ye, J. A novel relationship between elastic modulus and void ratio associated with principal stress for coral calcareous sand. *J. Rock Mech. Geotech. Eng.* **2023**, *in press*. [[CrossRef](#)]
42. Lv, Y.; Liu, J.; Xiong, Z. One-dimensional dynamic compressive behavior of dry calcareous sand at high strain rates. *J. Rock Mech. Geotech. Eng.* **2018**, *11*, 192–201. [[CrossRef](#)]
43. Wang, X.; Liu, J.; Cui, J.; Wang, X.; Shen, J.; Zhu, C. Particle breakage characteristics of a foundation filling material on island-reefs in the South China Sea. *Cons. Build. Mater.* **2021**, *306*, 124690. [[CrossRef](#)]
44. GB/T 50123-2019; Standard for Geotechnical Testing Method. Ministry of Housing and Urban-Rural Development of People's Republic of China, China Planning Press: Beijing, China, 2019. (In Chinese)
45. ASTM D2487; Standard Practice for Classification of soils for Engineering Purpose (Unified Soil Classification System). ASTM International: West Conshohocken, PA, USA, 2010. [[CrossRef](#)]
46. Shen, J.; Chen, X.; Wang, X.; Wang, X.; Qin, Y.; Wu, H. Compression responses and particle breakage of calcareous granular material in reclaimed islands. *Powder Technol.* **2023**, *418*, 118277. [[CrossRef](#)]
47. Wang, H.; Cui, Y.; Zhang, F.; Liu, J. Effect of grain breakage on the compressibility of soils. *Acta Geotech.* **2022**, *17*, 769–778. [[CrossRef](#)]
48. Wang, C.; Ding, X.; Yin, Z. Mechanical characteristics and particle breakage of coral sand under one-dimensional repeated loading. *Acta Geotech.* **2022**, *17*, 3117–3130. [[CrossRef](#)]
49. Ding, H.; Han, Z.; Li, Y.; Xie, W.; Fu, B.; Li, C.; Zhao, L. Particle breakage and its mechanical response in granular soils: A review and prospect. *Cons. Build. Mater.* **2023**, *409*, 133948. [[CrossRef](#)]
50. John, N.; Khan, I.; Kandalai, S.; Patel, A. Particle breakage in construction materials: A geotechnical perspective. *Cons. Build. Mater.* **2023**, *381*, 131308. [[CrossRef](#)]
51. Xie, K.; Li, T.; Chen, X.; Deng, Z. A novel method for determining the particle breakage contribution of high-speed railway graded aggregate and its application in vibratory compaction. *Case Stud. Constr. Mater.* **2023**, *19*, e02281. [[CrossRef](#)]
52. Zhang, S.; Wang, J.; Tong, C. A breakage matrix methodology to predict particle size evolution of calcareous sands. *Powder Technol.* **2022**, *407*, 117626. [[CrossRef](#)]
53. Hardin, B. Crushing of soils particles. *J. Geotech. Eng.* **1985**, *111*, 1177–1192. [[CrossRef](#)]
54. Mandelbrot, B. *The Fractal Geometry of Nature*; W. H. Freeman and Company: New York, NY, USA, 1982; Volume 51, pp. 286–287. [[CrossRef](#)]
55. Xu, Y. Explanation of scaling phenomenon based on fractal fragmentation. *Mech. Res. Commun.* **2005**, *32*, 209–220. [[CrossRef](#)]
56. Xie, Z.; Lü, X.; Zhang, Y.; Liu, X.; Ma, Y.; Xu, K. Study on mechanical property and breakage behavior of tunnel slag containing weak rocks as road construction material. *Cons. Build. Mater.* **2024**, *411*, 134164. [[CrossRef](#)]
57. Liu, S.; He, W.; Sun, Y.; Shen, C.; Wang, L. Analysis of the behavior of a high earth-core rockfill dam considering particle breakage. *Comput. Geotech.* **2023**, *157*, 105320. [[CrossRef](#)]
58. Li, M.; Zhang, J.; Guo, Y.; Pu, H.; Peng, Y. Influence of particle size distribution on fractal characteristics of waste rock backfill materials under compression. *J. Mater. Res. Technol.* **2022**, *20*, 2977–2989. [[CrossRef](#)]
59. Ari, A.; Akbulut, S. Effect of fractal dimension on sand-geosynthetic interface shear strength. *Powder Technol.* **2022**, *401*, 117349. [[CrossRef](#)]

Disclaimer/Publisher's Note: The statements, opinions and data contained in all publications are solely those of the individual author(s) and contributor(s) and not of MDPI and/or the editor(s). MDPI and/or the editor(s) disclaim responsibility for any injury to people or property resulting from any ideas, methods, instructions or products referred to in the content.